International Journal of Electrochemical Science 20 (2025) 101129

Contents lists available at ScienceDirect

International Journal of Electrochemical Science

journal homepage: www.editorialmanager.com/ijoes

Simultaneous Electrochemical Impedance Spectroscopy and Magnetic Resonance Imaging analysis of lithium-ion batteries

Andreas Markert [a], Max Morales [b], Christoph Guntlin [c], Hermann Nirschl [a], Gisela Guthausen [a,*]

[a] Karlsruhe Institute of Technology, Karlsruhe, Germany
[b] Eseo grande école d'ingénieurs, Angers, France
[c] Wyon AG, Appenzell Steinegg, Switzerland

ARTICLE INFO

Keywords:
Magnetic Resonance Imaging (MRI)
Electrochemical Impedance Spectroscopy (EIS)
Lithium-ion-batteries
Simultaneous measurement

ABSTRACT

Electrochemical Impedance Spectroscopy and Magnetic Resonance Imaging (MRI) were measured simultaneously on Lithium-Ion batteries. The motivation for developing this measurement method was the following: While Electrochemical Impedance Spectroscopy provides integral information on processes in the battery, MRI adds spatially resolved information on structures and their changes in the battery on a microscopic length scale. This offers combined and more comprehensive information on microscopic and integral levels. A significant benefit of simultaneous measurement is that the battery is in the same state as well as that it allows continuous measurement of a specific battery thus avoiding replacements and rest times when exchanging parts of the experiments. Comparative measurements of Electrochemical Impedance Spectroscopy, performed in parallel to MRI and outside of the MRI setup, however, require optimal decoupling of the electromagnetic fields involved in both techniques. The current version shows only minor differences in the impedances measured below 20 Hz. On the other hand, images were acquired with and without parallel Electrochemical Impedance Spectroscopy, the images show the same structural features. Differences are on the noise level of the MRI measurement. The combination of results of both techniques allows for a thorough detection and identification of the batteries behavior. For example, in the case of two fresh batteries, increased resistance could be assigned to inhibited ionic transport paths due to a misplaced separator. In aged and defective batteries, the combination of both techniques revealed the loss of electrolyte to be the main source of degradation.

1. Introduction

Electrochemical Impedance Spectroscopy (EIS) is often used in battery characterization. It allows for monitoring the electrochemical processes in batteries, described by their time constants and their influence on impedance $Z(f)$ [1–5]. The investigated cell is subjected to alternating current or voltage of a given frequency in EIS. The response of the cell is measured to calculate $Z(f)$. Inductance in connecting cables or additional resistances due to bad connections need to be avoided to measure $Z(f)$ unambiguously. However, differentiation of processes is not always straightforward due to overlapping time constants and unspecific responses. Equivalent circuit models (ECM) are often used for data interpretation based on circuit elements to model the impedance of the cell, ascribing a physical meaning to the individual elements.

Nuclear Magnetic Resonance (NMR) is a multifaceted analytical tool applied also in battery research [6–10]. Spectroscopy was used for the identification of different stages of lithium intercalation, also in *in-operando* experiments. NMR compatible batteries were built [11–17]. The electrolyte decomposition was investigated accordingly: Carbonate-based electrolytes were stored with different amounts of water, NMR revealed the decomposition dynamics [18,19]. PFG NMR is known to reliably measure diffusion coefficients of liquids, here the different components in the battery's electrolyte [20–24]. Relaxometry reveals solid-state ion dynamics [25–27] and cathode decomposition [28].

Magnetic Resonance Imaging (MRI) is known to deliver spatially resolved information about structures and velocities and is used in this work. In battery research, it was applied, for example, to investigate dendrite formation [29] and the lithium gradients during charge and discharge [28,30,31]. The technique is noninvasive, allowing for

* Corresponding author.
E-mail address: gisela.guthausen@kit.edu (G. Guthausen).

https://doi.org/10.1016/j.ijoes.2025.101129
Received 22 May 2025; Received in revised form 4 July 2025; Accepted 15 July 2025
Available online 16 July 2025

in-operando measurements.

The simultaneous measurements of EIS and MRI was realized and will be the focus of this paper. Simultaneous measurements are highly desirable as they ensure that the results of both measurements are not just of the same battery but also at the same state; without electrochemical relaxation or changes to the resistance of the EIS channels due to changed contact. Earlier studies successfully combined NMR spectroscopy with EIS [32,33]. MRI was combined with EIS for investigating solid electrolytes in symmetric lithium/lithium cells [34]. As a first example, the MRI experiments here will focus on the ^{1}H nuclei to correlate the microscopic structural elements of a Li-ion battery in form of the electrolyte distribution with the macroscopic, integral electrochemical view of the same battery in the same state.

2. Experimental

2.1. Investigated lithium-ion batteries

The investigated cells were produced by Wyon (Fig. 1). A total of 9 batteries were produced, five of which showed low or fluctuating voltages. They are equipped with one planar pair of electrodes separated by a stack of glass fiber separators (height before assembly 0.65 mm each). This leads to a larger volume of the electrolyte, which is the primarily accessible component of the battery in an MRI experiment. The electrolyte consists of carbonates as solvents, some additives and 1 M $LiPF_6$. The cathode active material is lithium cobalt oxide, and the anode is a graphite electrode. The cell's outer dimensions are 9 mm in diameter and 5.6 mm in height (Fig. 1d). The cells were cycled two times at 0.1 C after formation cycles.

One battery that passed this test and one that did not were investigated using the simultaneous EIS and ^{1}H MRI approach. Only two cells were investigated as the main aim of this work was to investigate the feasibility of the simultaneous measurement approach.

The batteries used in this study do not use metallic vapor barriers. Such barriers would shield the radio frequency pulses of the MRI experiments (200 MHz). Shielding of the rf pulses reduces, depending on the barrier's material and thickness, the signal intensity and hamper MRI measurements on the inner structure of a battery. Nevertheless, the impact of the state of charge of the battery could be monitored exploiting its impact on the magnetic field [35–38].

2.2. Measurement setup

MRI experiments were performed on an Avance HD3 spectrometer (Fig. 2d background) with a superwide bore 4.7 T superconducting magnet (Fig. 2d foreground). The gradient system Mirco2.5 was used together with a MicroWB40 MRI probe (Fig. 2b). A 25 mm inner diameter ^{1}H-birdcage was used in quadrature mode (all parts from Bruker Ettlingen). The experiments were performed within the Paravision 6.0.1 software environment. The RARE (Rapid Acquisition with Relaxation Enhancement) pulse sequence was used for fast imaging, the parameters are summarized in Table 1.

The batteries were positioned in a home-built battery holder made from polyether ether ketone (Fig. 2c). The orientation of the batteries electrodes was chosen to be orthogonal to the main magnetic field $\boldsymbol{B}_0$ of the MRI's magnet (Fig. 1, Fig. 2). This orientation is preferred as it prevents the current collectors and electrodes from shielding the MRI's radio frequency pulses [39–41]. Additionally this orientation allows for the twisted connecting wires to be of equal length, this allows for a highly reproducible setup. The battery in the holder is placed into a 25 mm MRI birdcage (Fig. 1b).

The battery contacts are connected via copper leave springs which are cleaned regularly to ensure a good electrical contact. A perfect electric connection is essential for reliable EIS. Thus, aged connections

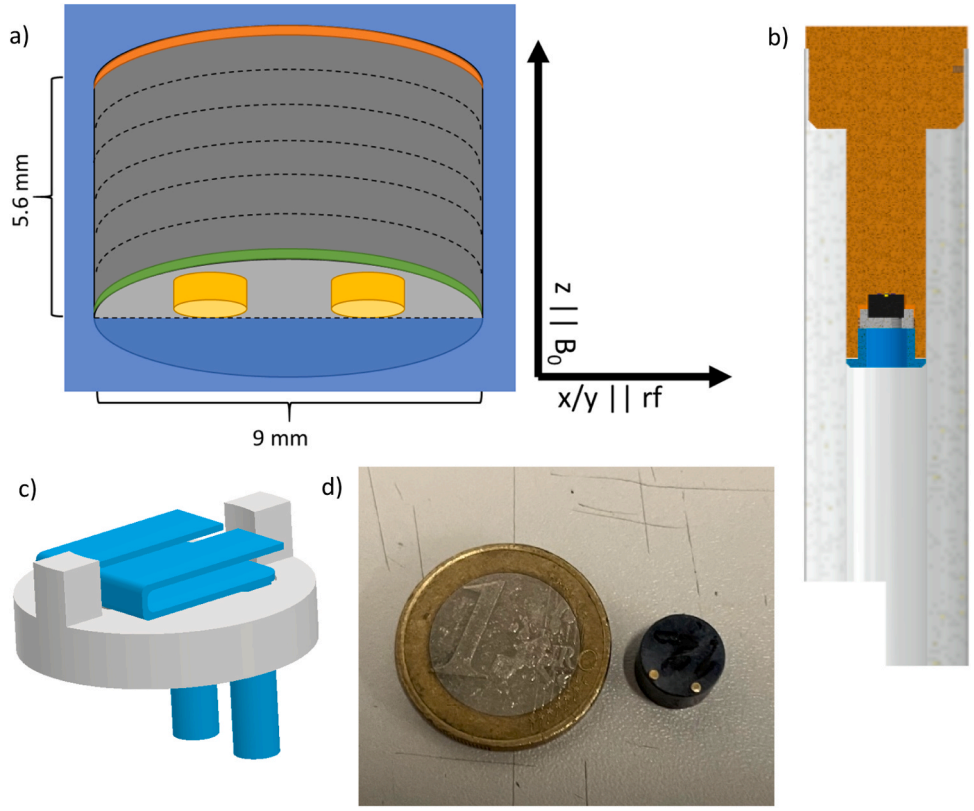

Fig. 1. a) Schematic of the MRI-compatible battery with cathode (orange) and anode (green). Dotted lines represent the separators. The arrow defines the *z* direction and the direction of $\boldsymbol{B}_0$ in MRI. b) Position of the battery (black) in the battery holder (brown) and the MRI probe (grey). The battery is kept in place by the lid (c) which is fastened by a screw (blue, middle). d) Image of the battery.

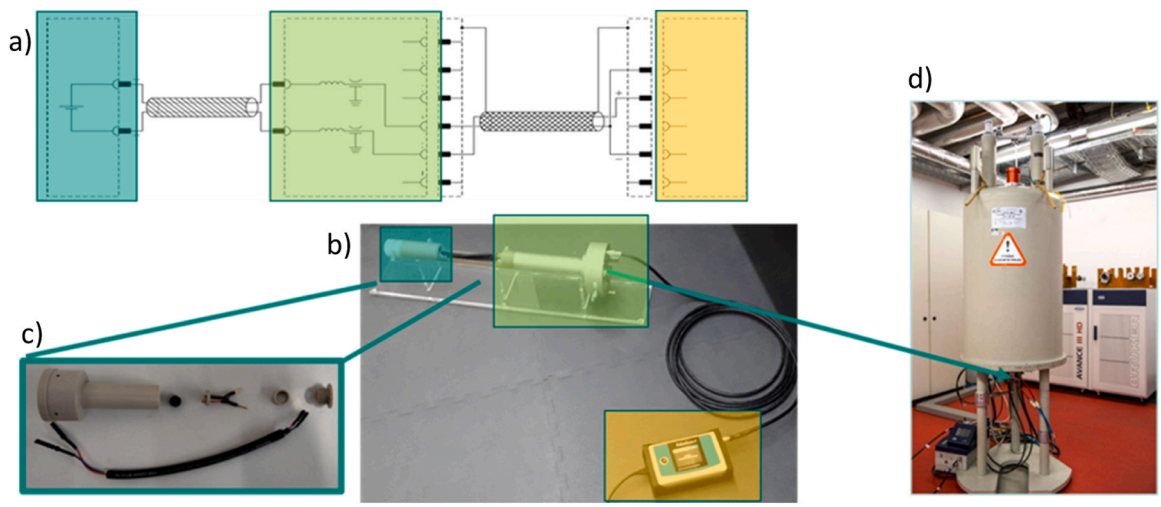

Fig. 2. a) Wiring of the experimental setup of the combined experiments. Colored boxes show (from left to right) the battery, the wiring inside the MRI probe and the potentiostat. b) The MRI probe was connected to the potentiostat, here outside of the magnet. c) Disassembled battery holder with the twisted cable connecting the battery to the MRI probe. d) NMR magnet with the inserted MRI probe (bottom) and the spectrometer in the background.

Table 1
Parameters of the RARE MRI experiments.

Parameter	Value
RARE Factor [-]	5
τ_e [ms]	2.2
T_r [s]	5
n_s [-]	16
Slice thickness [mm]	0.5
px x px [- x -]	128 × 128
FoV [mm × mm]	10 × 10
Measurement time [min]	25

led to deterioration of the measurement quality over time. A short-twisted cable connects the battery to the MRI probe, which also needs to be of excellent quality over time. A five-meter double-shielded cable, also with two twisted wires, connects the probe to the potentiostat. The shielding ensures that the probe and the potentiostat are grounded to the same place, which leads to a reduction of statistical noise. The length of the cable is given by the geometry of the large stray field of the super-wide bore magnet, as the potentiostat must be placed outside the 5 G line of the magnetic field.

A PalmSense 4 potentiostat/galvanostat was used in potentiostatic mode running with the software PStrace 5.8. (both PalmSense). Frequencies ranged from 1 Hz to 100 kHz. A hold phase of 20 min was applied before each measurement in which the open circuit voltage was measured.

3. Results and discussion

The two measurement techniques, both using high-frequency electromagnetic fields, influence each other. Both, ^{1}H MRI at 200 MHz and EIS at frequencies of 1 Hz to 100 kHz in this study, may be hampered by electromagnetic interferences, which needs to be investigated and minimized to the level of the respective noise levels of both measurement methods [32,33]. The optimized experimental setup satisfies this condition to a large extent.

3.1. Influence of MRI on EIS

The wires connecting the battery to the MRI probe (Fig. 2) run along $\boldsymbol{B}_0$ and perpendicular to $\boldsymbol{B}_1$, they might act as an antenna [32,33]. The picked-up noise could influence the EIS results vice versa. No impact of the static magnetic field is to be expected as all wires run parallel to the main magnetic field $\boldsymbol{B}_0$. Positioning of the battery in an MRI was thoroughly investigated for example in [39].

Two EIS experiments were performed to investigate this possible influence on the optimized setup: The first experiment was made with the rf probe inside the magnet. An MRI experiment was started at approximately the same time as the EIS measurement was started. The same EIS experiment was repeated with the MRI probe outside of the magnet and its stray field. The same 5 m cable was used to connect the probe. It was ensured that this rather long cable doesn't act as an additional inductance in the EIS measurement.

The real- and the negative imaginary part of the impedance $Z(f)$ are identical over a wide range of frequencies (Fig. 3a). Minor differences between the two measurement setups were seen at frequencies below 20 Hz. The Nyquist plot (Fig. 3b) reflects processes in the battery: Region I is attributed to solid state diffusion named diffusive tail at large Re $(Z(f))$ ($f \in [1,\ 3]$ Hz, marked by I in Fig. 3b). The semi-circle ($f \in [3,\ 400]$ Hz, region II) is attributed to charge-transfer resistance and the double layer capacitance of the electrodes. The semi-circle at higher frequencies ($f \in \left[400,\ 10^5\right]$ Hz, marked by III in Fig. 3b) is often attributed to processes related to the Solid Electrolyte Interface (SEI). Region IV reflects the overall bulk resistance [4,42].

EIS measurements were performed in- and outside of the MRI equipment. The differences between the two measurements are mostly visible in the diffusive tail (marked by I in Fig. 3). This indicates that EIS data measured simultaneous to MRI measurements need to be analyzed in detail at the larger frequencies of the diffusive tail [3,43].

3.2. Influence of EIS on MRI

The wires connecting both, the battery and the potentiostat, to the MRI probe potentially work as an antenna in both directions. Imperfect masses and loops are known to introduce noise in MRI measurements. Coupling of EIS to a battery and performing simultaneously MRI could introduce errors in form of artefacts or increased statistical noise in the MR images. This is partly compensated by twisted pair cables, as the induced magnetic fields connected with an electrical current should cancel out; the impact of EIS on MRI nevertheless needs to be investigated.

Fig. 4 shows ^{1}H MR images of the same cell, (a) without the 5 m cable connected to the MRI probe and (b) measured simultaneously with EIS. The false color scale represents the MRI intensity in each voxel. The signal primarily depends on the number of observed nuclei in a voxel and the relaxation times T_1, T_2. No signal from the cell casing was

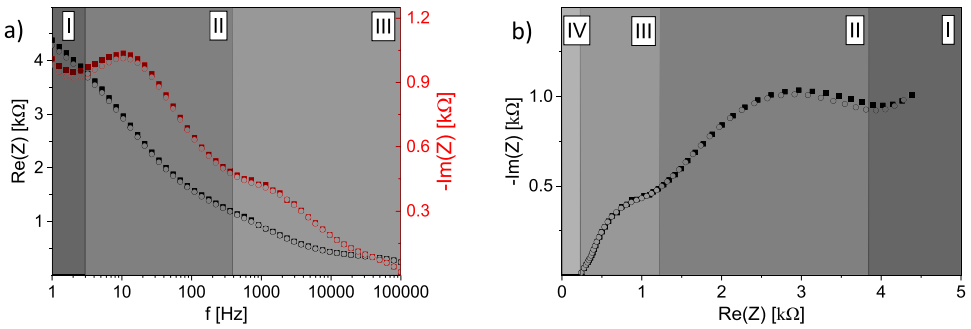

Fig. 3. EIS on an MRI compatible battery cell **in** (o) and **outside** (■) of the MRI equipment: a) real part Re(*Z*) (black symbols/left *y*-axis) and negative imaginary part -Im(*Z*) (red symbols/right *y*-axis) as a function of frequency *f*. b) Nyquist plot (filled symbols: EIS only, open symbols: combined experiments. Area I: diffusive tail, associated with solid state lithium diffusion in the solid materials. Area II: mid frequency semi-circle most often associated with the charge-transfer at the electrodes. Area III: high frequency semi-circle associated with the interfacial layer (SEI). Area IV: bulk resistance.

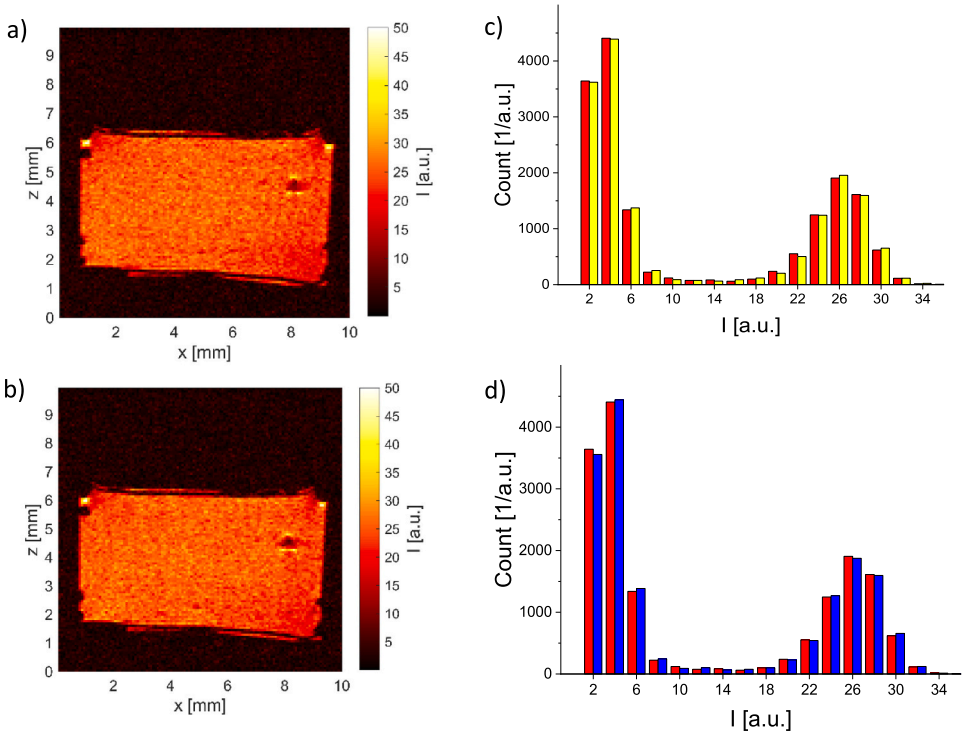

Fig. 4. ^{1}H MRI sagittal images of an MRI compatible lithium-ion battery: a) potentiostat disconnected b) MR image acquired simultaneously with an EIS measurement. c) Histograms of the images a) (red) and b) (yellow). d) Histograms of a) (red) and another image (not shown, blue) measured under identical circumstances showing the statistical noise in an MRI measurement. Connected bars in the histograms represent the value in the middle of them.

observed as T_2 of hard polymers is typically much shorter than that of liquids and leads to an already vanished signal on the time scale of a RARE experiment. The intensity thus represents a map of the electrolyte in each voxel. As the voxel size of the measured image is 78 µm × 78 µm in plane with 0.5 mm slice thickness, the pores of the separator are not resolved, and the electrolyte filled separators appear rather homogeneous with indications of the layered structure.

The dark lines near $z = 1.5$ and 6.5 mm in both images are the electrodes including the current collector. A small amount of electrolyte is found on the outer sides of both electrodes. At $(x, z) = (8, 4.5)$ mm a gas bubble shows up: An area of rather lower signal intensity is surrounded by three spots of large signal intensity. These spots arise in MRI when two substances of different magnetic susceptibility, like electrolyte and gas, are in contact, while one of the substances has a spherical symmetry. This leads to local field inhomogeneities at the interfaces. At $z = 6$ mm two points of higher signal intensity can be seen with the same origin.

All the structures are at the same positions in both measurements, and no additional artifacts are visible in the measurements combined with EIS measurement. Regarding the signal-to-noise ratio, detailed information can be extracted from the histograms (Fig. 4c): only small differences are visible between the red bars, representing the image without EIS and connectors, and the yellow bars, representing the image measured simultaneous with EIS.

To contextualize these differences, histograms of two repeatedly measured images without a connection to the potentiostat were calculated (Fig. 4d), which reflect the repeatability of an MRI experiment. The differences between the two histograms are in the same order of magnitude as the differences in the former comparison. This leads to the conclusion that the differences in the combined experiments are in the order of statistical random noise. Simultaneous measurements of EIS and MRI are thus possible with the described setup and no influence above noise can be seen in the MRI.

3.3. Comparison of two cells of the same batch

One battery that passed the final control at Wyon and one that did not were measured via MRI and EIS simultaneously. The Nyquist plots of EIS on both cells (Figs. 5a and 5c) exhibit same principal shapes, composed of the two semicircles followed by a diffusive tail. However, the defective cell shows a much larger bulk resistance R_b: 250 Ω compared to 85 Ω for the fully functional cell. Both semi-circles appear much more pronounced in the case of the defective cell, this is especially true for the first semi-circle, which is often attributed to processes at the solid electrolyte interface (SEI) [44].

The ^{1}H MR images (Figs. 5b and 5d) add microscopic information to this integral information: Questions about the influence of the battery's structure on the electric performance can be addressed and answered. First, the image of the properly functional battery is interpreted: Electrolyte can be seen above the upper current collector and below the lower current collector. The area of the electrolyte/separator appears apart from a few gas bubbles rather homogeneous, note discontinuities are visible on the length scale of the MRI. Gas bubbles on the lower electrode might be linked to the larger size of the second semi-circle in EIS when compared to the first semi-circle. The bubbles might lead to reduced area for charge transfer between electrode and electrolyte to happen [4].

In contrast, the defective cell shows less electrolyte on the outer sides of the electrodes in the ^{1}H images. This might be correlated to the larger size of both semi-circles (Fig. 5c compared to Fig. 5a), as the lower amount of electrolyte may lead to uncovered electrode surface. The second separator (counted from the bottom up) seems to be displaced along *y* direction, discontinuities are apparent. This indicates that ionic transport paths are distorted in this cell. This is in accordance with the comparatively larger R_b of this cell. Furthermore, the second semi-circle is more complete and the separation between second semi-circle and diffusive tail clearer. This is probably caused by a lower time constant of the processes leading to the second semi-circle in the case of the defective battery [42].

3.4. Comparison of fresh cells and cells after a storage period

Measurements on the battery that passed the producer's tests were repeated after it was stored for 18 months. First, the EIS results: Only low voltages below 0.1 V were measured, and charging was impossible. The impedance (Figs. 6a and 6c) of the battery drastically increased over all frequencies as well. R_b increased to 8100 Ω. Furthermore, the initially observed two semi-circles cannot be distinguished anymore. The diffusive tail, however, is still visible, and the values of -Im(*Z*) monotonously increase with Re(*Z*) in contrast to Fig. 5c.

^{1}H MRI images (Figs. 6b and 6d) give insights on a micro scale into degradation: The signal intensity is much smaller than it was before the storage period, and the separator layers soaked with electrolyte are separated by dark lines. The two factors imply that some electrolyte must be lost, either due to reactions [18], leakage or similar processes. The remaining electrolyte might be localized in the separator layers via capillary forces. The electrolyte-poor borders between the separators now hinder the ions transport between the electrodes in the battery which explains the enormous increase in resistance and impedance [45–47]. Additionally, some deformation of the upper separator sheets can be seen as well as a total lack of electrolyte in the lower left corner of the stored battery.

The electrolyte area without the electrodes was cropped from the two images in order to compare their structure in more detail. The cropped area of the aged cell is smaller due to the shape which leads to the smaller maximum in the cumulative distribution. The cumulative distribution of the image intensities in those cropped areas (Fig. 6e) highlight the larger signal intensity of the fresh cells. The distribution of the fresh cell (black) shows less counts at small intensities assigned to few gas bubbles while the distribution of the aged shows a lot of signal in that intensity range due to many areas of low electrolyte concentration.

The second battery (Fig. 5) was also measured before (Figs. 7a and 7b) and after storage over 18 months (Figs. 7c and 7d). The results are similar to the discussed results of the first battery. Again, only small voltages below 0.1 V were measured, and charging was not possible. The Nyquist plots change from two distinct semi-circles followed by a

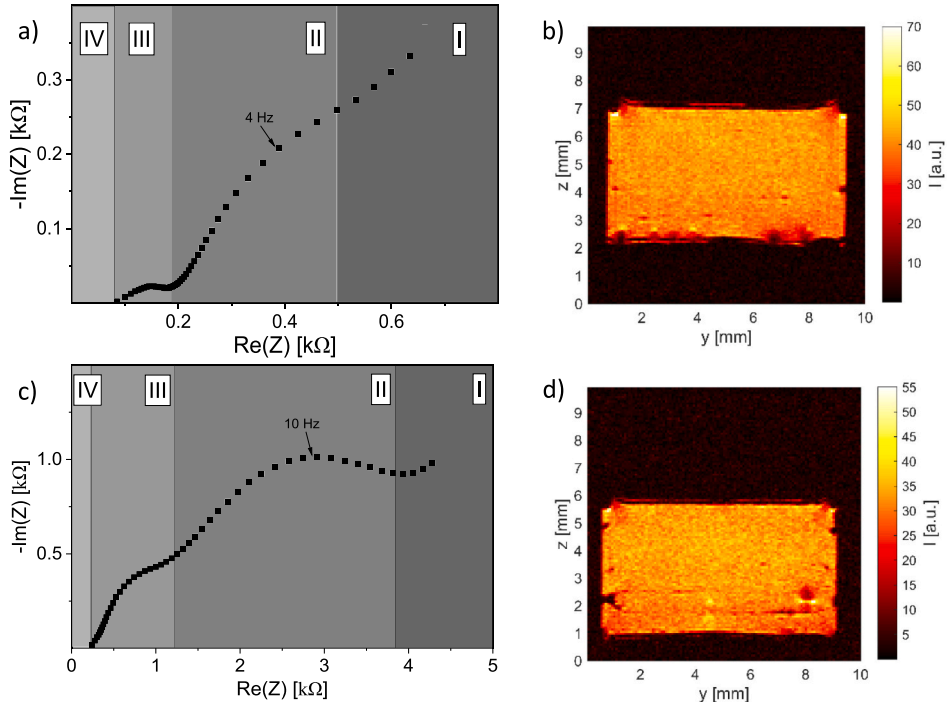

Fig. 5. a) and b) Nyquist plot and ^{1}H MR image of a cell that passed the final tests. c) and d) Nyquist plot and ^{1}H MRI image of a cell that didn't pass the final tests. Area I: diffusive tail, associated with solid state lithium diffusion in the solid materials. Area II: mid frequency semi-circle often associated with the charge-transfer at the electrodes. Area III: high frequency semi-circle associated with the interfacial layer (SEI). Area IV: bulk resistance.

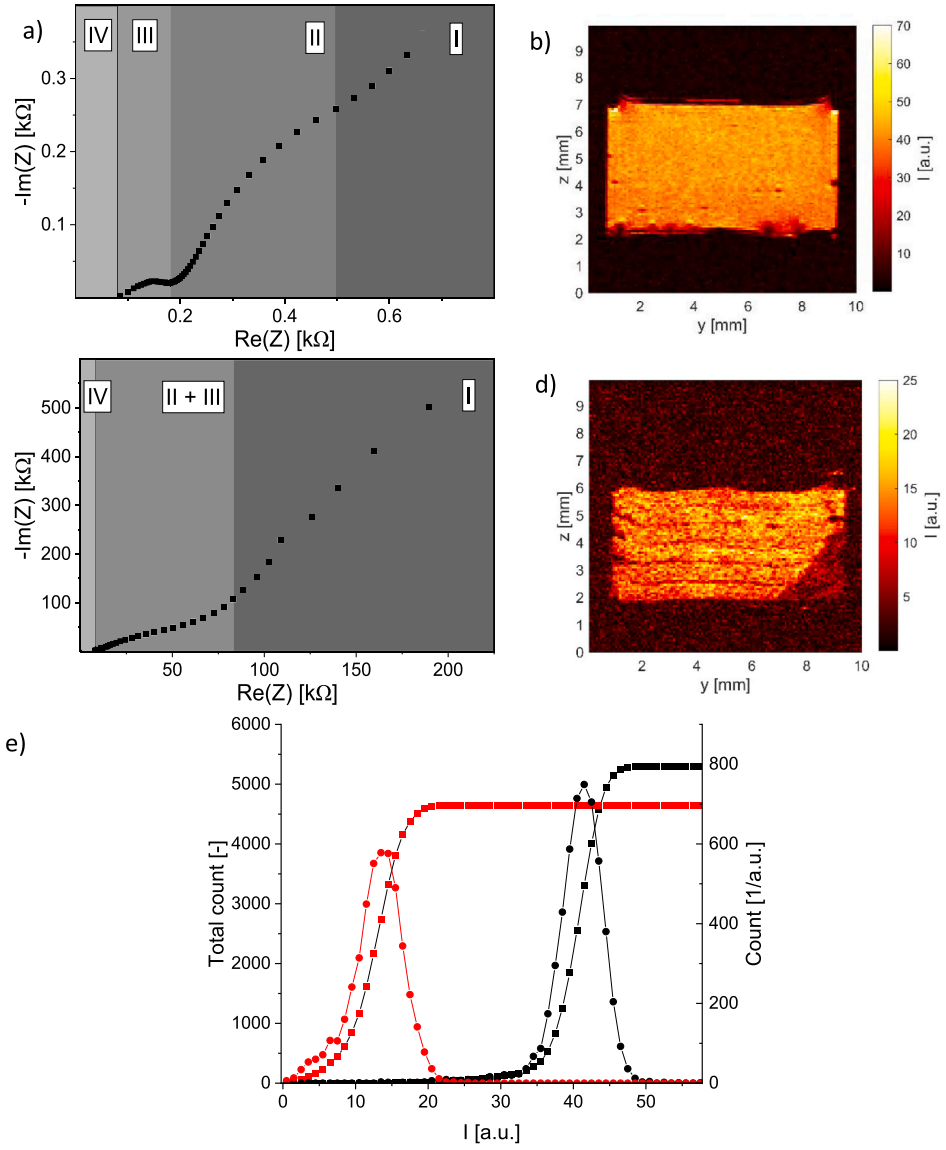

Fig. 6. a) and b) Nyquist plot and ^{1}H-MR image of a fresh cell that passed the final tests. c) and d) Nyquist plot and ^{1}H MR image of the same cell after 18 months of storage. Areas are defined as above. e) Intensity histograms (circles) and cumulative distributions (squares) of image b) (here: black) and d) (here: red). The lines serve as guides to the eyes.

diffusive tail to roughly one semi-circle followed by a diffusive tail, while the impedance increases at all frequencies. R_b increased to 4800 Ω in this case. The onset of the tail is also far less distinct in the aged cell compared to the fresh cell and can be explained by a shorter time constant of the second process or the semi-circle representing another process [45,46].

The ^{1}H MRI image of the cell after storage (Fig. 7d) again shows a reduced signal intensity compared to the fresh cell (Fig. 7b), the medium signal intensity is also smaller compared to the aged cell in Fig. 6d, some dark lines between individual separator layers are visible at $y = 9$ mm but are not as distinct as in Fig. 6d. The general reduction in signal intensity implies that even more electrolyte has been lost being the main reason for the degradation of this cell [44].

The same procedure of cropping was applied on the MR images of this battery. The cumulative distribution of the image intensities (Fig. 7e) again shows the larger signal intensity of the fresh cell. The shape of distributions are more similar compared to that of the first battery. Again, the lower amount of electrolyte left after aging leads to a significant shift in the intensity histogram.

4. Conclusions

Non-invasive Magnetic Resonance Imaging (MRI) and Electrochemical Impedance Spectroscopy (EIS) on Lithium-ion batteries give correlated insight into microscopic structural properties and integral electrotechnically relevant measures. Both rely on electromagnetic waves, but on different frequencies. Mutual influences of MRI and EIS were therefore investigated on an optimized setup. It was shown that a commercial MRI and a potentiostat allows - together with dedicated wiring - for the simultaneous measurement of EIS and MRI on MRI compatible batteries. Only marginal mutual influences of the techniques were found. Small differences between EIS measured simultaneous to an MRI scan and EIS measured separately were found at frequencies smaller than 20 Hz while no differences at higher frequencies were noticeable. On the other hand, ^{1}H MR images measured simultaneously to EIS showed no significant differences above experimental noise to images measured separately.

First experiments on experimental cells built by Wyon suggest that the combination of both techniques is a useful tool to investigate the electrotechnical state and the structure inside batteries simultaneously

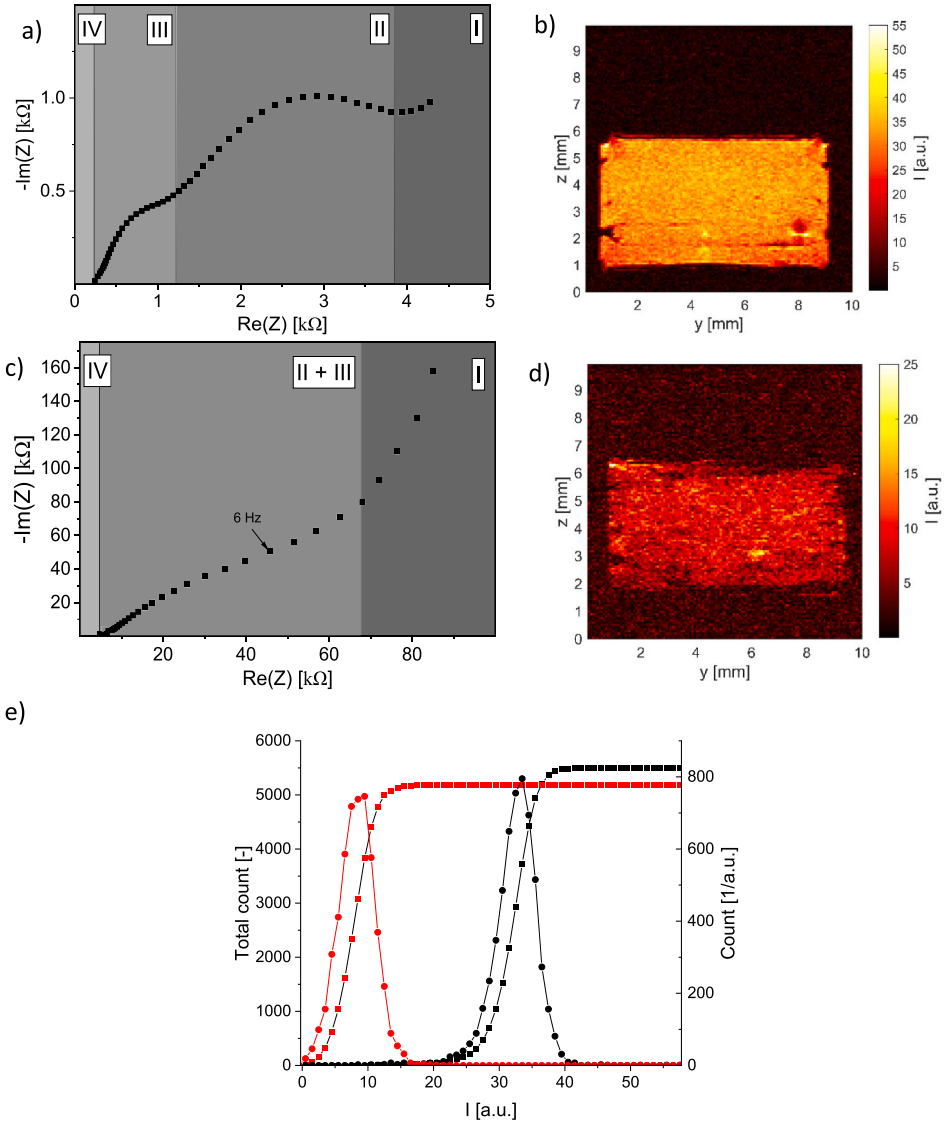

Fig. 7. a) and b) Nyquist plot and ^{1}H MR image of a fresh cell that didn't pass the final tests. c) and d) Nyquist plot and ^{1}H MR image of the same cell after 18 months in storage. Areas are defined as above. e) Intensity histograms (circles) and cumulative distributions (squares) of image b) (here: black) and d) (here: red). The lines serve as guides to the eyes.

while allowing for a correlated view on the results on an integral and a microscopic level. It was possible to attribute increased resistance in one battery to a misplaced separator inside the separator stack. Investigations after a long storage period of the same cells revealed that a loss of electrolyte is the most likely degradation mechanism and showed that the electrolyte mainly is in the glass fiber separator layers. To complement the investigations, ^{7}Li MRI will be explored in future investigations to correlate both, structure and impedance with ion distribution and state [28].

Author Contributions

The manuscript relies on contributions of all authors. All authors have given approval to the final version of the manuscript.

CRediT authorship contribution statement

Andreas Markert: Writing – original draft, Visualization, Investigation, Data curation, Conceptualization. **Max Morales:** Writing – review & editing, Investigation. **Christoph Guntlin:** Writing – review & editing, Resources. **Hermann Nirschl:** Writing – review & editing, Supervision, Resources, Project administration, Funding acquisition. **Gisela Guthausen:** Writing – review & editing, Writing – original draft, Supervision, Software, Resources, Project administration, Methodology, Funding acquisition, Conceptualization.

Declaration of Competing Interest

The authors declare that they have no known competing financial interests or personal relationships that could have appeared to influence the work reported in this paper.

Acknowledgements

The authors thank the German Research Foundation (DFG) for financial support of the instrumental facility Pro^{2}NMR. Furthermore, DFG funded the cooperative work within GRK 2218 SiMET—Simulation of mechano-electro-thermal processes in lithium-ion batteries, Project no.: 281041241). We thank the Pro^{2}NMR group members for fruitful discussions. The authors thank Stefanie Margiotta-Neu and Raphael Kräling for their work in improving the experimental setup and the technical facilities at the Institute of Mechanical Process Engineering

and Mechanics (MVM) namely Olaf Jörg for the manufacturing of the cell holder.

References

[1] J. Asenbauer, T. Eisenmann, M. Kuenzel, A. Kazzazi, Z. Chen, D. Bresser, The success story of graphite as a lithium-ion anode material – fundamentals, remaining challenges, and recent developments including silicon (oxide) composites, Sustain. Energy Fuels 4 (2020) 5387–5416, https://doi.org/10.1039/D0SE00175A.

[2] P. Vadhva, J. Hu, M.J. Johnson, R. Stocker, M. Braglia, D.J.L. Brett, A.J.E. Rettie, Electrochemical impedance spectroscopy for all-solid-state batteries: theory, methods and future outlook, ChemElectroChem 8 (2021) 1930–1947, https://doi.org/10.1002/celc.202100108.

[3] M.D. Levi, D. Aurbach, Diffusion coefficients of lithium ions during intercalation into graphite derived from the simultaneous measurements and modeling of electrochemical impedance and potentiostatic intermittent titration characteristics of thin graphite electrodes, J. Phys. Chem. B 101 (1997) 4641–4647, https://doi.org/10.1021/jp9701911.

[4] L.A. Middlemiss, A.J.R. Rennie, R. Sayers, A.R. West, Characterisation of batteries by electrochemical impedance spectroscopy, Energy Rep. 6 (2020) 232–241, https://doi.org/10.1016/j.egyr.2020.03.029.

[5] S.B. Aziz, T.J. Woo, M.F.Z. Kadir, H.M. Ahmed, A conceptual review on polymer electrolytes and ion transport models, J. Sci. Adv. Mater. Devices 3 (2018) 1–17, https://doi.org/10.1016/j.jsamd.2018.01.002.

[6] S. Krachkovskiy, M.L. Trudeau, K. Zaghib, Application of magnetic resonance techniques to the *in situ* characterization of Li-ion batteries: a review, Materials 13 (2020) 1694, https://doi.org/10.3390/ma13071694.

[7] C.P. Grey, J.M. Tarascon, Sustainability and in situ monitoring in battery development, Nat. Mater. 16 (2017) 45–56, https://doi.org/10.1038/nmat4777.

[8] N. Leifer, D. Aurbach, S.G. Greenbaum, NMR studies of lithium and sodium battery electrolytes, Prog. Nucl. Magn. Reson. Spectrosc. 142-143 (2024) 1–54, https://doi.org/10.1016/j.pnmrs.2024.02.001.

[9] P.P.R.M.L. Harks, F.M. Mulder, P.H.L. Notten, In situ methods for Li-ion battery research: a review of recent developments, J. Power Sources 288 (2015) 92–105, https://doi.org/10.1016/j.jpowsour.2015.04.084.

[10] S. Wiemers-Meyer, M. Winter, S. Nowak, A battery cell for in situ NMR measurements of liquid electrolytes, Phys. Chem. Chem. Phys. 19 (2017) 4962–4966, https://doi.org/10.1039/C6CP08653E.

[11] C. Grosu, C. Panosetti, S. Merz, P. Jakes, S. Seidlmayer, S. Matera, R.-A. Eichel, J. Granwehr, C. Scheurer, Revisiting the storage capacity limit of graphite battery anodes: spontaneous lithium overintercalation at ambient pressure, PRX Energy 2 (2023) 013003, https://doi.org/10.1103/PRXEnergy.2.013003.

[12] M. Letellier, F. Chevallier, M. Morcrette, *In situ* ^{7}Li nuclear magnetic resonance observation of the electrochemical intercalation of lithium in graphite; 1st cycle, Carbon 45 (2007) 1025–1034, https://doi.org/10.1016/j.carbon.2006.12.018.

[13] M. Letellier, F. Chevallier, F. Béguin, *In situ* ^{7}Li NMR during lithium electrochemical insertion into graphite and a carbon/carbon composite, J. Phys. Chem. Solids 67 (2006) 1228–1232, https://doi.org/10.1016/j.jpcs.2006.01.088.

[14] M. Letellier, F. Chevallier, F. Béguin, E. Frackowiak, J.-N. Rouzaud, The first *in situ* ^{7}Li NMR study of the reversible lithium insertion mechanism in disorganised carbons, J. Phys. Chem. Solids 65 (2004) 245–251, https://doi.org/10.1016/j.jpcs.2003.10.022.

[15] F. Chevallier, M. Letellier, M. Morcrette, J.M. Tarascon, E. Frackowiak, J. N. Rouzaud, F. Béguin, *In situ* ^{7}Li-nuclear magnetic resonance observation of reversible lithium insertion into disordered carbons, Electrochem. Solid-State Lett. 6 (2003) A225, https://doi.org/10.1149/1.1612011.

[16] F. Chevallier, F. Poli, B. Montigny, M. Letellier, *In situ* ^{7}Li nuclear magnetic resonance observation of the electrochemical intercalation of lithium in graphite: second cycle analysis, Carbon 61 (2013) 140–153, https://doi.org/10.1016/j.carbon.2013.04.078.

[17] K. Märker, C. Xu, C.P. Grey, *Operando* NMR of NMC811/graphite lithium-ion batteries: structure, dynamics, and lithium metal deposition, J. Am. Chem. Soc. 142 (2020) 17447–17456, https://doi.org/10.1021/jacs.0c06727.

[18] S. Wiemers-Meyer, M. Winter, S. Nowak, Mechanistic insights into lithium ion battery electrolyte degradation – a quantitative NMR study, Phys. Chem. Chem. Phys. 18 (2016) 26595–26601, https://doi.org/10.1039/C6CP05276B.

[19] S. Wiemers-Meyer, S. Jeremias, M. Winter, S. Nowak, Influence of battery cell components and water on the thermal and chemical stability of LiPF6 based lithium ion battery electrolytes, Electrochim. Acta 222 (2016) 1267–1271, https://doi.org/10.1016/j.electacta.2016.11.100.

[20] S.A. Krachkovskiy, J.D. Bazak, S. Fraser, I.C. Halalay, G.R. Goward, Determination of mass transfer parameters and ionic association of LiPF6: organic carbonates solutions, J. Electrochem. Soc. 164 (2017) A912–A916, https://doi.org/10.1149/2.1531704jes.

[21] S.A. Krachkovskiy, A.D. Pauric, I.C. Halalay, G.R. Goward, Slice-selective NMR diffusion measurements: a robust and reliable tool for in situ characterization of ion-transport properties in lithium-ion battery electrolytes, J. Phys. Chem. Lett. 4 (2013) 3940–3944, https://doi.org/10.1021/jz402103f.

[22] K. Hayamizu, S. Tsuzuki, S. Seki, Y. Umebayashi, Nuclear magnetic resonance studies on the rotational and translational motions of ionic liquids composed of 1-ethyl-3-methylimidazolium cation and bis(trifluoromethanesulfonyl)amide and bis(fluorosulfonyl)amide anions and their binary systems including lithium salts, J. Chem. Phys. 135 (2011) 084505, https://doi.org/10.1063/1.3625923.

[23] K. Hayamizu, S. Seki, H. Miyashiro, Y. Kobayashi, Direct in situ observation of dynamic transport for electrolyte components by NMR combined with electrochemical measurements, J. Phys. Chem. B 110 (2006) 22302–22305, https://doi.org/10.1021/jp065616a.

[24] K.S. Han, J.D. Bazak, Y. Chen, T.R. Graham, N.M. Washton, J.Z. Hu, V. Murugesan, K.T. Mueller, Pulsed field gradient nuclear magnetic resonance and diffusion analysis in battery research, Chem. Mater. 33 (2021) 8562–8590, https://doi.org/10.1021/acs.chemmater.1c02891.

[25] J. Langer, V. Epp, P. Heitjans, F.A. Mautner, M. Wilkening, Lithium motion in the anode material LiC_6 as seen via time-domain ^{7}Li NMR, Phys. Rev. B 88 (2013) 094304, https://doi.org/10.1103/PhysRevB.88.094304.

[26] K. Volgmann, V. Epp, J. Langer, B. Stanje, J. Heine, S. Nakhal, M. Lerch, M. Wilkening, P. Heitjans, Solid-state NMR to study translational Li ion dynamics in solids with low-dimensional diffusion pathways, Z. für Phys. Chem. 231 (2017) 1215–1241, https://doi.org/10.1515/zpch-2017-0952.

[27] A. Markert, T. Rudszuck, M. Gerasimov, U. Krewer, H. Nirschl, G. Guthausen, Lithium mobility in graphite anodes at different states of charge as observed by NMR, J. Phys. Chem. C (2025), https://doi.org/10.1021/acs.jpcc.4c08394.

[28] R. Balbierer, P. Seegert, S. Herberger, T. Wetzel, H. Nirschl, G. Guthausen, Investigation of transverse relaxation rate distribution via magnetic resonance imaging: impact of electrode formation, Energy Technol. (2021) 2000571–2000578, https://doi.org/10.1002/ente.202000579.

[29] A.J. Ilott, M. Mohammadi, H.J. Chang, C.P. Grey, A. Jerschow, Real-time 3D imaging of microstructure growth in battery cells using indirect MRI, Proc. Natl. Acad. Sci. 113 (2016) 10779–10784, https://doi.org/10.1073/pnas.1607903113.

[30] S.A. Krachkovskiy, J.M. Foster, J.D. Bazak, B.J. Balcom, G.R. Goward, *Operando* mapping of Li concentration profiles and phase transformations in graphite electrodes by magnetic resonance imaging and nuclear magnetic resonance spectroscopy, J. Phys. Chem. C 122 (2018) 21784–21791, https://doi.org/10.1021/acs.jpcc.8b06563.

[31] S. Klamor, K. Zick, T. Oerther, F.M. Schappacher, M. Winter, G. Brunklaus, 7Li in situ ^{1}D NMR imaging of a lithium ion battery, Phys. Chem. Chem. Phys. 17 (2015) 4458–4465, https://doi.org/10.1039/C4CP05021E.

[32] S.A. Kayser, A. Mester, A. Mertens, P. Jakes, R.-A. Eichel, J. Granwehr, Long-run in operando NMR to investigate the evolution and degradation of battery cells, Phys. Chem. Chem. Phys. 20 (2018) 13765–13776, https://doi.org/10.1039/C8CP01067F.

[33] S.C. Adediwura, N. Mathew, J. Schmedt auf der Günne, Combining NMR and impedance spectroscopy in situ to study the dynamics of solid ion conductors, J. Mater. Chem. A 12 (2024) 15847–15857, https://doi.org/10.1039/D3TA06237F.

[34] K. Romanenko, L.Y. Jin, P. Howlett, M. Forsyth, In situ MRI of operating solid-state lithium metal cells based on ionic plastic crystal electrolytes, Chem. Mater. 28 (2016) 2844–2851, https://doi.org/10.1021/acs.chemmater.6b00797.

[35] A.J. Ilott, M. Mohammadi, C.M. Schauerman, M.J. Ganter, A. Jerschow, Rechargeable lithium-ion cell state of charge and defect detection by in-situ inside-out magnetic resonance imaging, Nat. Commun. 9 (2018) 1776, https://doi.org/10.1038/s41467-018-04192-x.

[36] M. Mohammadi, E.V. Silletta, A.J. Ilott, A. Jerschow, Diagnosing current distributions in batteries with magnetic resonance imaging, J. Magn. Reson. 309 (2019) 106601, https://doi.org/10.1016/j.jmr.2019.106601.

[37] K. Romanenko, P.W. Kuchel, A. Jerschow, Accurate visualization of operating commercial batteries using specialized magnetic resonance imaging with magnetic field sensing, Chem. Mater. 32 (2020) 2107–2113, https://doi.org/10.1021/acs.chemmater.9b05246.

[38] K. Romanenko, A. Jerschow, Distortion-free inside-out imaging for rapid diagnostics of rechargeable Li-ion cells, Proc. Natl. Acad. Sci. 116 (2019) 18783–18789, https://doi.org/10.1073/pnas.1906976116.

[39] I. Serša, U. Mikac, A study of MR signal reception from a model for a battery cell, J. Magn. Reson. 294 (2018) 7–15, https://doi.org/10.1016/j.jmr.2018.06.013.

[40] A.J. Ilott, S. Chandrashekar, A. Klöckner, H.J. Chang, N.M. Trease, C.P. Grey, L. Greengard, A. Jerschow, Visualizing skin effects in conductors with MRI: 7Li MRI experiments and calculations, J. Magn. Reson. 245 (2014) 143–149, https://doi.org/10.1016/j.jmr.2014.06.013.

[41] M.M. Britton, Magnetic resonance imaging of electrochemical cells containing bulk metal, Chemphyschem 15 (2014) 1731–1736, https://doi.org/10.1002/cphc.201400083.

[42] W. Choi, H.-C. Shin, J.M. Kim, J.-Y. Choi, W.-S. Yoon, Modeling and applications of electrochemical impedance spectroscopy (EIS) for lithium-ion batteries, J. Electrochem. Sci. Technol. 11 (2020) 1–13, https://doi.org/10.33961/jecst.2019.00528.

[43] U. Tröltzsch, O. Kanoun, H.-R. Tränkler, Characterizing aging effects of lithium ion batteries by impedance spectroscopy, Electrochim. Acta 51 (2006) 1664–1672, https://doi.org/10.1016/j.electacta.2005.02.148.

[44] P. Iurilli, C. Brivio, V. Wood, On the use of electrochemical impedance spectroscopy to characterize and model the aging phenomena of lithium-ion batteries: a critical review, J. Power Sources 505 (2021) 229860, https://doi.org/10.1016/j.jpowsour.2021.229860.

[45] S.M. Kuzovchikov, V.V. Zefirov, V.S. Neudachina, T.K. Zakharchenko, A. L. Zybkovets, A.A. Nikiforov, D.I. Gusak, A. Reveguk, M.S. Kondratenko, L. V. Yashina, D.M. Itkis, Electrolyte refilling as a way to recover capacity of aged

lithium-ion batteries, J. Power Sources 601 (2024) 234257, https://doi.org/10.1016/j.jpowsour.2024.234257.
[46] X. Lai, Y. Li, R. Fang, P. Dong, Y. Zheng, Z. Li, Experimental investigation of the influence of electrolyte loss and replenishment on the critical performances of cylindrical lithium-ion cells, J. Energy Storage 52 (2022) 104951, https://doi.org/10.1016/j.est.2022.104951.
[47] J. Vetter, P. Novák, M.R. Wagner, C. Veit, K.C. Möller, J.O. Besenhard, M. Winter, M. Wohlfahrt-Mehrens, C. Vogler, A. Hammouche, Ageing mechanisms in lithium-ion batteries, J. Power Sources 147 (2005) 269–281, https://doi.org/10.1016/j.jpowsour.2005.01.006.